Schuck *et al. Microstructures* 2024;4:2024047
DOI: 10.20517/microstructures.2024.33

Microstructures

Review

Open Access

Check for updates

On the thermal expansion of the tetragonal phase of $MAPbI_3$ and $MAPbBr_3$

Götz Schuck[1], **Daniel M. Többens**[1], **Susan Schorr**[1,2]

[1]Helmholtz-Zentrum Berlin für Materialien und Energie, Berlin 14109, Germany.
[2]Institut für Geologische Wissenschaften, Freie Universität Berlin, Berlin 12249, Germany.

Correspondence to: Dr. Götz Schuck, Helmholtz-Zentrum Berlin für Materialien und Energie GmbH, Hahn-Meitner-Platz 1, Berlin 14109, Germany. E-mail: goetz.schuck@helmholtz-berlin.de

How to cite this article: Schuck G, Többens DM, Schorr S. On the thermal expansion of the tetragonal phase of $MAPbI_3$ and $MAPbBr_3$. *Microstructures* 2024;4:2024047. https://dx.doi.org/10.20517/microstructures.2024.33

Received: 31 Mar 2024 **First Decision:** 9 May 2024 **Revised:** 2 Jun 2024 **Accepted:** 20 Jun 2024 **Published:** 9 Aug 2024

Academic Editor: Andrea Sanson **Copy Editor:** Fangling Lan **Production Editor:** Fangling Lan

Abstract

Based on previously published research, the structural response of the tetragonal hybrid perovskite crystal structure of $MAPbX_3$ [MA: $[CH_3NH_3]^+$, methylammonium; X = I, Br] to thermal expansion is reviewed here. From an averaged crystal structure perspective, the tetragonal perovskite structure of $MAPbI_3$ and $MAPbBr_3$, based on diffraction data, shows apparent Pb-X bond length shortening and apparent shrinkage of the $[PbX_6]$ octahedra with increasing temperature. At the same time, these apparent observations, and hence the thermal expansion, are related to the progressive phase transformation towards the cubic structure, as the lattice parameters respond to a shear stress that couples to the order parameters, and this coupling is predicted by group theory and thus aims to explain precisely the apparent negative thermal expansion-like effects. A different picture emerges for the thermal expansion when considering the very localized structure, since neither a shortening of the Pb-X bond lengths nor a shrinking of the $[PbX_6]$ octahedra is observed with pair distribution function analysis, and the presence of orthorhombic short-range order in the tetragonal and cubic perovskite structures is assumed in published studies. The compared extended X-ray absorption fine structure studies, which also map the local structure and provide the "true" bond distance, show no lead-halide bond length shortening with temperature. The perpendicular mean square relative displacement has been determined. Therefore, a comparison of the tension and bond expansion effects in both perovskites can be made. In the orthorhombic phase of $MAPbI_3$ and $MAPbBr_3$, positive expansion and negative tension of the lead-halide bond are almost balanced. After transitioning to the tetragonal phase, the equilibrium shifts toward negative tension. This suggests that both hybrid perovskites have tighter lead-halide bonds and less rigid $[PbX_6]$ octahedra in the tetragonal phase than in the low temperature perovskite crystal structure.

Keywords: Hybrid perovskites, thermal expansion, local structure, pair distribution function (PDF) analysis, extended X-ray absorption fine structure (EXAFS), tension effect

INTRODUCTION

Due to their optoelectronic properties (high optical absorption coefficients, narrow-band bright photoluminescence, tuneable bandgaps, low exciton binding energies, and long-range carrier diffusion)[1-3], hybrid perovskites are promising materials for applications in photovoltaics[4,5]. Hybrid perovskites of the general form $MAPbX_3$ (MA: $[CH_3NH_3]^+$, methylammonium; X = I, Br) such as $MAPbI_3$ and $MAPbBr_3$, undergo phase transformations from the cubic high-temperature aristo-type structure (space group $Pm\bar{3}m$) first to a tetragonal structure (space group $I4/mcm$, $T_{c,\ MAPbI3}$ = 330 K and $T_{c,\ MAPbBr3}$ = 236 K) and finally to an orthorhombic low-temperature structure (space group $Pnma$, $T_{c,\ MAPbI3}$ = 160 K and $T_{c,\ MAPbBr3}$ = 149 K) in which the MA molecule is less disordered[6,7]. In the cubic and tetragonal phase, only disordered positions for the MA molecule can be observed with diffraction methods due to the fast jump-rotation of the MA molecule (ps relaxation times and THz relaxation frequencies)[8]. In the low-temperature phase, the MA molecule also jump-rotates, but much slower (ns relaxation times and GHz relaxation frequencies)[8]. Due to the interaction between the strong MA molecule dynamics and the rigidity of the $[PbX_6]$ octahedra framework structure, it is not surprising that liquid-crystal duality is increasingly employed in the description of hybrid perovskites[9,10]. In a new classification, the existing dynamic aspects are added to the crystal structure description[11]. Thus, the tetragonal $I4/mcm$ room-temperature structure might now be described with the extended Glazer notation $a^d a^d b^-$ and the cubic $Pm\bar{3}m$ aristo-type structure with $a^d a^d a^d$ (in this new notation, d corresponds to the dynamic tilt, which indicates that the corresponding octahedra oscillate between two positions (positive and negative amplitude)). In this context, the quantitative analysis of the structural dynamics in time and space from molecular dynamics (MD) simulations of perovskite crystals by Liang *et al.* is noteworthy[12]. Recent experimental work by Weadock *et al.* also attempts to describe the nature of the dynamic local ordering of $MAPbI_3$ and $MAPbBr_3$ in the cubic phase by a combination of single-crystal diffuse scattering, neutron inelastic spectroscopy, and MD simulations[13]. In this investigation, a remarkable collective dynamics consisting of a network of local, two-dimensional, circular regions of dynamically tilting lead halide octahedra (lower symmetry), giving rise to long-range intermolecular $CH_3NH_3^+$ correlations, has been identified[13]. The presence of orthorhombic short-range order in the tetragonal and cubic structures of $MAPbX_3$ has also been experimentally confirmed by studies of the pair distribution function (PDF)[14-17]. As stated by Simenas *et al.* in their comprehensive review of hybrid perovskites[18], referring to the work of Weadock *et al.*[13], “the presence of such low symmetry correlated octahedral distortions at the nanoscale could be related to the observed ferroelectric effects in this compound”, but we will not discuss the ferroic properties in our selective review and refer to existing experimental work[19-21] and review publications[22-25] on this controversial topic. Due to the temperature-dependent changes in the crystal structures, local ordering phenomena and structural dynamics, hybrid perovskites exhibit a number of remarkable thermal properties that are particularly important for their application in photovoltaics[26]. For example, the thermal expansion of the tetragonal room temperature structure of $MAPbI_3$ is relatively high and strongly anisotropic. In the temperature range from 308 to 324 K, Jacobsson *et al*. observed a negative linear thermal expansion coefficient $\alpha_{[001],\ tetragonal} = -106 \times 10^{-6}\ K^{-1}$ in the [001] direction and a positive linear thermal expansion coefficient $\alpha_{[100],\ tetragonal} = 132 \times 10^{-6}\ K^{-1}$ in the [100] direction[27]. Thus, the thermal expansion corresponds more to a soft material, for instance, a polymer such as polypropylene ($\alpha = 118 \times 10^{-6}\ K^{-1}$)[28], than, for example, typical representatives of semiconductor technology such as silicon ($\alpha = 2.6 \times 10^{-6}\ K^{-1}$)[29]. In keeping with soft materials, the thermal conductivity of hybrid perovskites is very low, with Ge *et al.* observing an extremely low thermal conductivity of $\kappa = 0.3\ Wm^{-1}K^{-1}$ for $MAPbI_3$[30]. The extreme thermal properties of hybrid perovskites cause difficulties because photovoltaics require close coupling with many different materials that have completely different thermal properties than hybrid perovskites. This affects both manufacturing and application stability and longevity of the thin film photovoltaic devices, making strain engineering important[31]. The observed thermal properties of hybrid perovskites indicate strong anharmonic interactions, with increasing evidence that the anharmonic properties of the lead-halide bond in particular[32] play a prominent role when wanting to better understand the extremely soft hybrid perovskite lattice. A very well-suited method to investigate the anharmonic properties of the lead-halide bond is extended X-ray absorption fine structure (EXAFS) analysis in combination with crystallographic structure determination[33,34]. Since EXAFS can be used to determine the relative atomic vibrations, including the correlation of atomic motion, in the form of the parallel and perpendicular mean square relative displacement (MSRD), the bond-bending and bond-stretching effective force constants and frequencies of the Pb-X bonds are directly accessible[33,34]. The perpendicular MSRD can be determined by comparing the "true" distance of certain atomic pairs, in this case, lead-halide, obtained by fitting the EXAFS spectra with a simulation, with the "apparent" distance measured by diffractometric means[34].

In a selective short review, the thermal expansion of the tetragonal phase of $MAPbI_3$ and $MAPbBr_3$ is discussed here on the basis of published work in which results from X-ray diffraction (XRD) and EXAFS are combined[6,7]. Based on the results of the structural investigations on the temperature-dependent XRD data of $MAPbI_3$ and $MAPbBr_3$, the thermal expansion in the tetragonal phases is analyzed and described by linear thermal expansion coefficients. The temperature dependence of these thermal expansion coefficients is then quantified for $MAPbI_3$. For both components, the phase transformation from the tetragonal to the cubic perovskite structure is described by the corresponding order and strain parameters. Based on the PDF analysis of $MAPbBr_3$ by Bernasconi *et al*., the thermal expansion is discussed from a local order perspective[16]. Finally, the results of temperature-dependent EXAFS analyses of $MAPbI_3$ and $MAPbBr_3$ are compared and discussed.

DISCUSSION

Apparent shrinkage of [PbX_6] octahedra and Pb-X bond lengths changes in the tetragonal phases of $MAPbI_3$ and $MAPbBr_3$

Two previous temperature-dependent crystallographic investigations of $MAPbI_3$ from Schuck *et al*.[6] and of $MAPbBr_3$ from Weadock *et al*.[7] are compared and discussed in relation to the observed volume changes of the [PbX_6] octahedra and the changes in Pb-X bond lengths. In the following, we will focus on the tetragonal phase [Figure 1] and the transition to the cubic structure by looking at the behavior of the [PbX_6] octahedra network in dependence on temperature [Figure 2]. Powder samples of $MAPbI_3$ were measured by Schuck *et al*. using synchrotron XRD as a function of temperature, and the resulting diffractograms were refined using the Rietveld method. The MA molecule geometry was taken from the previous density functional theory (DFT) optimization and treated as rigid[35]. The results of the structure refinements of $MAPbI_3$[6] agree with previous temperature-dependent studies[36-38].

The volume of $MAPbI_3$ increases with temperature over the whole temperature range (volumetric thermal expansion coefficient $\alpha_{V,\ orthorhombic} = 90 \times 10^{-6}\ K^{-1}$ and $\alpha_{V,\ tetragonal} = 119 \times 10^{-6}\ K^{-1}$). Based on the lattice constants for a pseudo-cubic cell from Schuck *et al*., a negative linear thermal expansion coefficient of $\alpha_{[001],\ tetragonal} = -23.3(3) \times 10^{-6}\ K^{-1}$ in the [001] direction and a positive linear thermal expansion coefficient of $\alpha_{[100],\ tetragonal} = 75(3) \times 10^{-6}\ K^{-1}$ in the [100] direction can be determined for $MAPbI_3$ (temperature range 220-260 K) [Figure 3A][6]. The differences between these linear thermal expansion coefficients of Schuck *et al*. and those of Jacobsson *et al*. are due to the different temperature ranges used to determine the gradient[6,27]. Jacobsson *et al*. used a higher temperature range of 308 to 324 K. Figure 4 shows the percentage changes in Pb-X bond length expansion [Figure 4A] and the percentage changes in volume expansion [Figure 4B] from the onset of the tetragonal phase to higher temperatures[27]. In the tetragonal phase, the maximum thermal expansion at 300 K is +1.68% (compared to 160 K) for the whole volume and +2.14% for

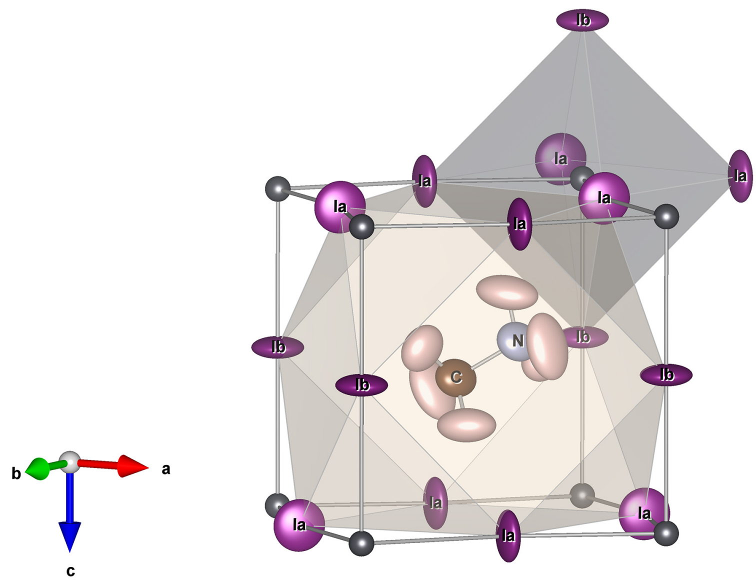

Figure 1. Detail of the tetragonal room-temperature structure of $MAPbI_3$ with its large iodine anisotropic temperature factors (ADPs) (their flat shape indicates a transverse displacement perpendicular to the Pb-I-Pb bonds and in the direction of the MA molecule), the coordination polyhedra of the MA molecule $[MAI_{12}]$, a cuboctahedron (light yellow), and one $[PbI_6]$ octahedra (light gray)[37]. The anisotropic shape and orientation of the halide ADPs are partly due to the strongly anharmonic metal-halide bond (see EXAFS section) and not only to the hydrogen bond between the MA and the halide atoms (formed between the jump rotations). In this representation of a single MA molecule, neither the 4-fold rotational axis nor the 2-fold rotational axis of the *I*4/*mcm* space group symmetry seems to exist for the molecule. However, since the MA molecule jump rotates[8] and there are, on average, eight MA molecule orientations in the cage, an average structure with *I*4/*mcm* symmetry is observed in diffraction.

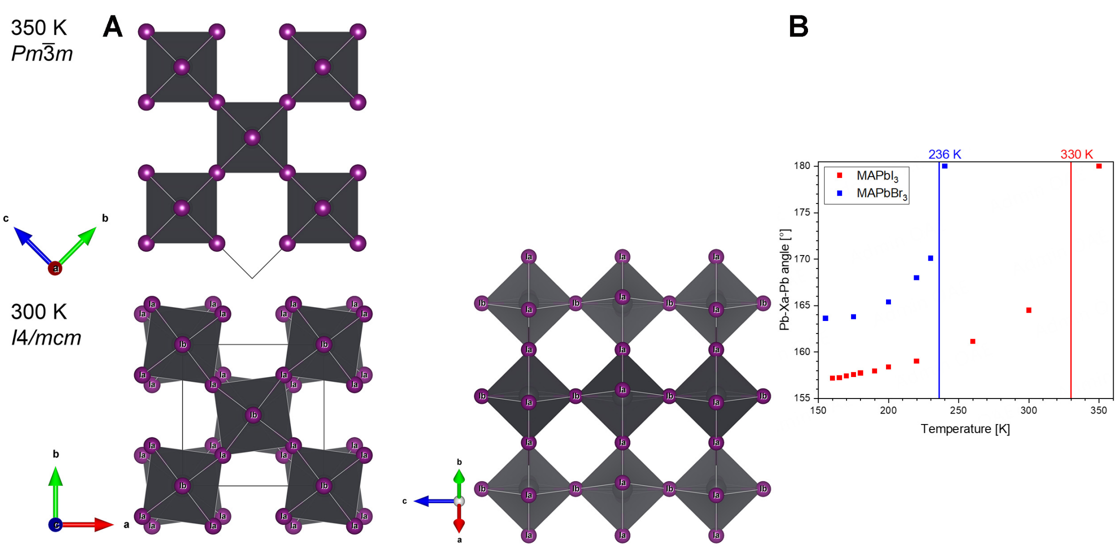

Figure 2. (A) The $[PbI_6]$ octahedra network of $MAPbI_3$ for the cubic high-temperature structure at 350 K[36] (top) and the tetragonal room-temperature structure at 300 K[37] (bottom). (B) Pb-Xa-Pb bond angle (octahedra tilt) of $MAPbI_3$ (red) and $MAPbBr_3$ (blue) in the tetragonal (solid symbols) and cubic phase (open symbols). Besides the data from Schuck *et al.*[6] and Weadock *et al.*[7], values for the cubic phase at 350 K of $MAPbI_3$ from Whitfield *et al.* are also given[36]. Adapted with permission from Schuck *et al.*[6]. Copyright 2022 American Chemical Society.

the $[MAI_{12}]$ cuboctahedra. In contrast, the negative thermal expansion (NTE) of the $[PbI_6]$ octahedra is -0.5%, corresponding to the negative change in average bond length, which is -0.17% smaller at 300 K

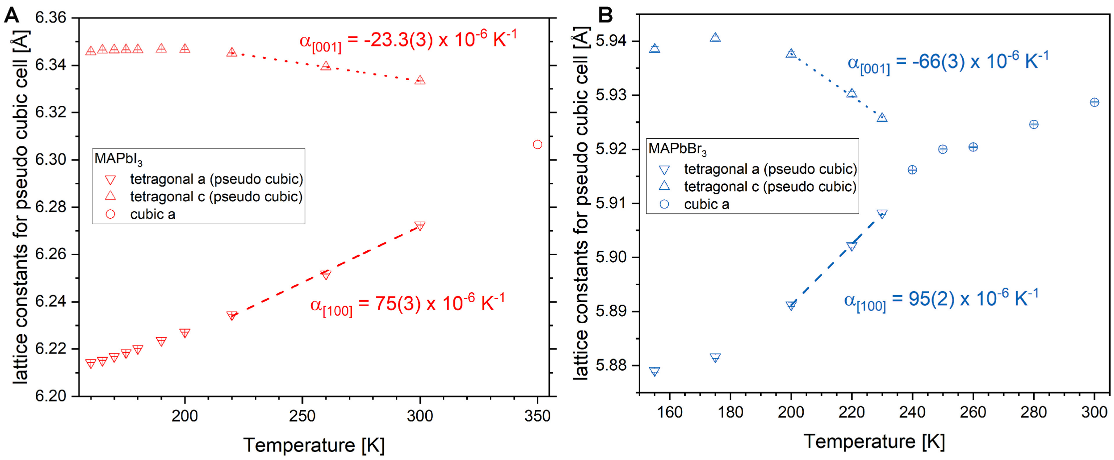

Figure 3. Temperature-dependent lattice constants for the tetragonal (pseudo-cubic) and cubic unit cell for (A) $MAPbI_3$ (cubic at 350 K from Whitfield *et al.*[36]) and (B) $MAPbBr_3$ based on the results of Schuck *et al.*[6] and Weadock *et al.*[7]. In both cases, the linear thermal expansion coefficients in direction [100] [positive thermal expansion (PTE)] and in direction [001] [negative thermal expansion (NTE)] are also given. Adapted with permission from Schuck *et al.*[6]. Copyright 2022 American Chemical Society.

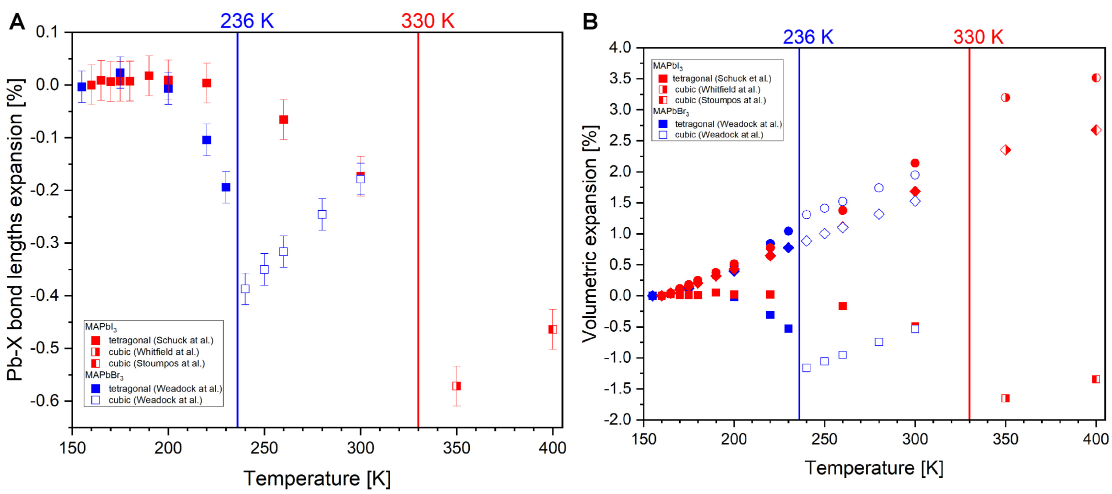

Figure 4. (A) Averaged Pb-X bond lengths expansion and (B) volumetric expansion of $MAPbI_3$ (red) and $MAPbBr_3$ (blue) in the tetragonal (solid symbols) and cubic phase (open and half-open symbols), the phase transformation temperature is indicated in each case (tetragonal to cubic). Besides the data from Schuck *et al.*[6] and Weadock *et al.*[7], values for the cubic phase of $MAPbI_3$ are also given from Whitfield *et al.*[36] (left half-open symbols) and Stoumpos *et al.*[38] (right half-open symbols). (B) In addition to the volume changes for the $[PbX_6]$ octahedra (squares), the volume changes for the total volume (diamond symbols) and the volume changes for the $[MAX_{12}]$ cuboctahedra (circles) are also given. Note: Both Pb-X bond lengths, i.e., the one along tetragonal c (Pb-Xb in Figure 2A) and the one in the tetragonal a-b plane (Pb-Xa in Figure 2A), become smaller in the tetragonal phase with increasing temperature. Both bond lengths (Pb-Xa and Pb-Xb) for $MAPbI_3$ and $MAPbBr_3$ are within the error bars of the averaged value Pb-X. Adapted with permission from Schuck *et al.*[6]. Copyright 2022 American Chemical Society.

compared to the value at 160 K. Based on the tetragonal lattice constants for a pseudo-cubic cell from Weadock *et al.*, which are available from their temperature-dependent single-crystal structure investigations [crystallographic information files (CIF) were made available][7], a NTE of $\alpha_{[001],\,tetragonal}$ = -66(3) × 10^{-6} K^{-1} in the [001] direction and a positive thermal expansion of $\alpha_{[100],\,tetragonal}$ = 95(2) × 10^{-6} K^{-1} in the [100] direction can be determined for $MAPbBr_3$ (for the temperature range 200-230 K) [Figure 3B]. As shown in Figure 4, a maximum thermal expansion at 240 K is observed for $MAPbBr_3$ in the tetragonal phase, analogous to the behavior of $MAPbI_3$. While the total volume of $MAPbBr_3$ and the $[MABr_{12}]$ cuboctahedra volume increase by +0.78% and +1.04%, respectively, the Pb-Br bond length decreases by -0.19% with a concomitant NTE of -0.53% for the $[PbBr_6]$ octahedra. In both $MAPbI_3$ and $MAPbBr_3$, the temperature-dependent negative changes in the partial volumes of the $[PbX_6]$ octahedra, on the one hand, and positive partial volume changes of the $[MAX_{12}]$ cuboctahedra, on the other hand, differ significantly from the change in the total volume in the tetragonal phase. While the $[MAX_{12}]$ cuboctahedra volume expands almost linearly with increasing temperature (greater expansion than total volume), the $[PbX_6]$ octahedra volume shrinks towards the cubic phase [Figure 4B]. A comparison with pressure-dependent data in the tetragonal phase would certainly also be interesting, but for $MAPbBr_3$ such data are not yet available[39] in the corresponding temperature and pressure range, and for $MAPbI_3$ a clearly different behavior of the tetragonal structure already occurs at 300 K in the range of 0.05 GPa (the $[PbI_6]$ octahedra become 0.15% smaller, and Pb-I shortens by 0.05%)[40], so that it cannot be excluded that phase transformations also occur at minimal pressures and a direct comparison of the mechanochemical sensitive[41] $MAPbI_3$ data is not readily possible.

Temperature-dependent linear thermal expansion coefficients and the Grüneisen tensor

The linear thermal expansion coefficients calculated for $MAPbI_3$ from the data of Schuck *et al.* differ significantly from the values of Jacobsson *et al.*[6,27]. This is not surprising since one linear fit obviously cannot describe the entire temperature range of the tetragonal phase. For this reason, the temperature dependence of the linear thermal expansion coefficients is investigated using the tetragonal lattice constants of Whitfield *et al.* [the lattice constants from temperature-dependent synchrotron powder XRD measurements of Whitfield *et al.* (figure 6C in Ref.[36]) have been digitized by us and are shown here in Figure 5A][36]. The temperature dependence of the linear thermal expansion coefficients [Figure 5B] can be approximately described for the PTE $\alpha_{[100]}$ with a linear behavior; an increase towards the cubic phase up to 97×10^{-6} K^{-1} is obtained. The NTE $\alpha_{[001]}$ can be described with a third-order polynomial and reaches a maximum value of -88×10^{-6} K^{-1} towards the cubic phase. Due to the temperature dependence of the two linear thermal expansion coefficients $\alpha_{[001]}$ and $\alpha_{[100]}$, the linear thermal expansion coefficient $\alpha_{[averaged]}$ determined from the averaged tetragonal lattice constant $a_{averaged} = ((2*a_{tet})+c_{tet})/3$ is more suitable for describing the thermal expansion as it has almost no temperature dependence. The value given by Whitfiled *et al.*[36] is to be multiplied by $1/L_0$ and then results in $\alpha_{[averaged]} = 42.4(4) \times 10^{-6}$ K^{-1} (dotted line in Figure 5B)[42]. It is common to describe thermal expansion properties of solids in Grüneisen parameters: NTE results in negative Grüneisen parameter γ.

In the case of the tetragonal crystal structure of hybrid perovskites, two independent Grüneisen parameters, $\gamma_{[100]}$ and $\gamma_{[001]}$, are related to the principal linear thermal expansion coefficients $\alpha_{[100]}$ and $\alpha_{[001]}$ via (according to Schorr *et al.*[43]):

$$\gamma_{[100]} = \frac{V_m}{C_p}[(c_{11}^S + c_{13}^S)\alpha_{[100]} + c_{13}^S\alpha_{[001]}]$$
$$\gamma_{[001]} = \frac{V_m}{C_p}[2c_{13}^S\alpha_{[100]} + c_{33}^S\alpha_{[001]}]. \quad (1)$$

where V_m is the molar volume, C_p is the molar specific heat at constant pressure, and the c_{ij} are the adiabatic elastic stiffness coefficients in this Grüneisen tensor (according to Haussühl and Kitaigorodskii)[44]. Using the tabulated c_{ij} values[45], a negative Grüneisen parameter $\gamma_{[001]}$ can only be expected near the phase transition to the cubic phase above 307 K [Figure 6A]. At lower temperatures, $\gamma_{[001]}$ is positive and the Grüneisen parameter $\gamma_{[100]}$ is always positive for $MAPbI_3$ [Figure 6B].

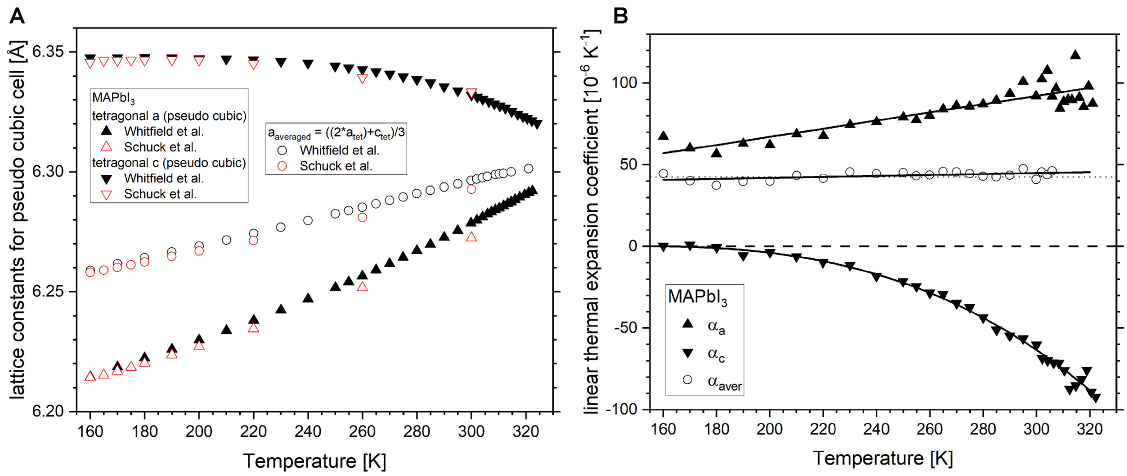

Figure 5. (A) Temperature-dependent tetragonal (pseudo-cubic) lattice constants according to Whitfield *et al.*[36] (black) and from Schuck *et al.*[6] (red). (B) Temperature dependence of the linear thermal expansion coefficients $\alpha_{[100]}$, $\alpha_{[001]}$, and $\alpha_{[averaged]}$ based on the lattice constants of Whitfield *et al.* [displayed in (A)][36]. $\alpha_{[100]}$: linear behavior; $\alpha_{[001]}$: third-order polynomial (solid lines). Adapted with permission from Schuck *et al.*[6]. Copyright 2022 American Chemical Society.

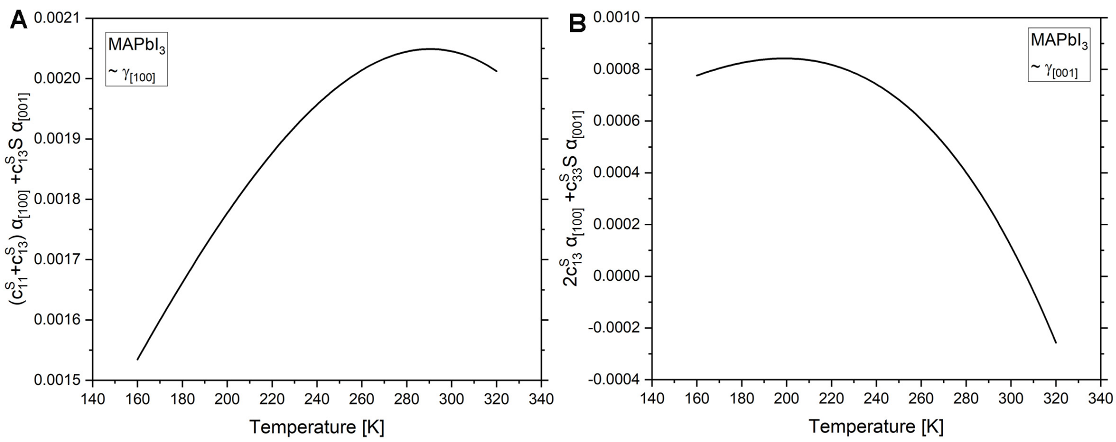

Figure 6. (A) Temperature-dependent values of $[2c^S_{13}\alpha_{[100]} + c^S_{33}\alpha_{[001]}] \sim \gamma_{[001]}$ and (B) temperature-dependent values of $[(c^S_{11} + c^S_{13})\alpha_{[100]} + c^S_{13}\alpha_{[001]}] \sim \gamma_{[100]}$. (A and B) for $MAPbI_3$ using the tabulated c_{ij} values from Feng *et al.*[45].

Tetragonal to the cubic phase transition

According to Whitfield *et al.*, the phase transition from the tetragonal to the cubic crystal structure in $MAPbI_3$ and $MAPbBr_3$ can be described by the temperature-dependent change of three degrees of freedom in the tetragonal structure: the rotational distortion caused by the change of the Pb-Ia-Pb angle (R_4^+), the strain caused by the thermal expansion (GM_1^+), and the strain caused by the tetragonal distortion (GM_3^+)[36].

The temperature-dependent changes of the three degrees of freedom were analyzed for $MAPbI_3$ and $MAPbBr_3$ using ISODISTORT (an internet-server tool for exploring structural phase transitions)[46] and are shown in Figure 7. The thermal expansion in the tetragonal phase discussed in the previous two sections is related to the progressive phase transformation towards the cubic structure, since the lattice parameters respond to a shear stress coupled to the order parameters (analyzed with ISODISTORT), and this coupling is predicted by a standard Landau theory treatment. The amplitude of the R_4^+ rotational mode, which is directly proportional to the cubic-tetragonal order parameter, can be fitted by the power law $R_4^+ \sim (T_c-T)^\beta$,

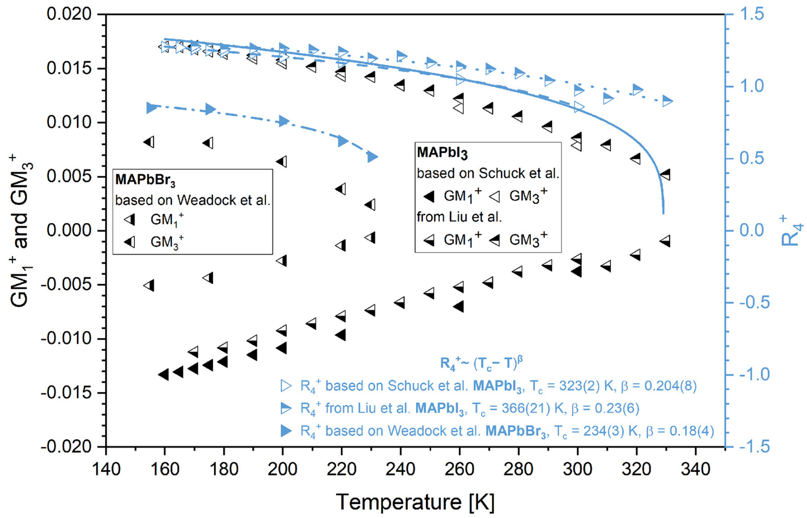

Figure 7. ISODISTORT analysis[46]. The phase transition from tetragonal to cubic, based on the data from Schuck *et al.*[6] and Liu *et al.*[47] for $MAPbI_3$ and based on the data from Weadock *et al.*[7] for $MAPbBr_3$ can be described by the temperature-dependent changes of the three degrees of freedom in the tetragonal structure: rotational distortion mode R_4^+ (blue color, legend on the right) and the two strain mode amplitudes (black color, legend on the left) GM_1^+ (thermal expansion) and GM_3^+ (tetragonal distortion (c-a)/c). Fit of the order parameter R_4^+ for $MAPbI_3$ based on the data from Schuck *et al.*[6] (blue dashed line) and fit for the data from Liu *et al.*[47] (blue dotted line), additional also the R_4^+ fit from Whitfield *et al.*[36] (figure 8A in Ref.[36]) is reproduced (T_c = 329.95 K and β = 0.26, solid blue line). Fit of the order parameter R_4^+ for $MAPbBr_3$ based on the data from Weadock *et al.* (blue dash-dotted line)[7].

where β is the critical exponent [Figure 7]. Both Whitfield *et al.*[36] and Liu *et al.*[47] conclude in their analysis that the tetragonal/cubic phase transition for $MAPbI_3$ can be characterized by a single order parameter and that its behavior as a function of temperature and spontaneous strain follows the form of a weakly first-order, nearly tricritical phase transition, which is consistent with the description of a standard Landau free energy function. The standard Landau theory treatment should then also explain the temperature-dependent behavior of the Pb-X bond lengths and the $[PbX_6]$ octahedra in the tetragonal phase towards the cubic structure, although it is worth noting that there is some variance in the description of the order parameter in the case of $MAPbI_3$ [Figure 7]. However, the differences between the R_4^+ data of Schuck *et al.*[6] and Weadock *et al.*[7] seem to be smaller.

Local structure of $MAPbI_3$ and $MAPbBr_3$ with atomic pair distribution function (PDF) analysis

The local atomic structure can be investigated by analyzing the total scattering from diffraction experiments[48,49], which, in contrast to XRD or neutron powder diffraction methods, use much shorter X-ray or neutron radiation wavelengths. In addition, total scattering measurements are generally made over a much larger scattering vector range (Q_{max} = 30 Å^{-1}) than in conventional XRD experiments (Q_{max} = 5 Å^{-1}). Besides Bragg scattering, total scattering includes diffusion scattering. The PDF can be used to analyze the total scattering, whereby a Fourier transformation of the measured total scattering must be carried out after extensive data reduction (including a thorough background correction)[48,49].

In the temperature-dependent pair correlation functions G(r) of $MAPbI_3$, it is, first of all, noticeable, as already noted by Whitfield *et al.*, that in a range up to about 4 Å, no discontinuous changes occur in the range from 10 to 350 K, but only a gradual broadening of G(r) towards high temperatures (see figure 4 in Ref.[36]), which is also especially the case in the range of the phase transformation from the orthorhombic to the tetragonal structure (o/t)[36]. This range up to 4 Å, which does not change discontinuously, corresponds to the Pb-X bond distances. The situation is different for the range from 4 Å to larger distances, where a discontinuous change in G(r) in the temperature range of the o/t phase transformation is observed.

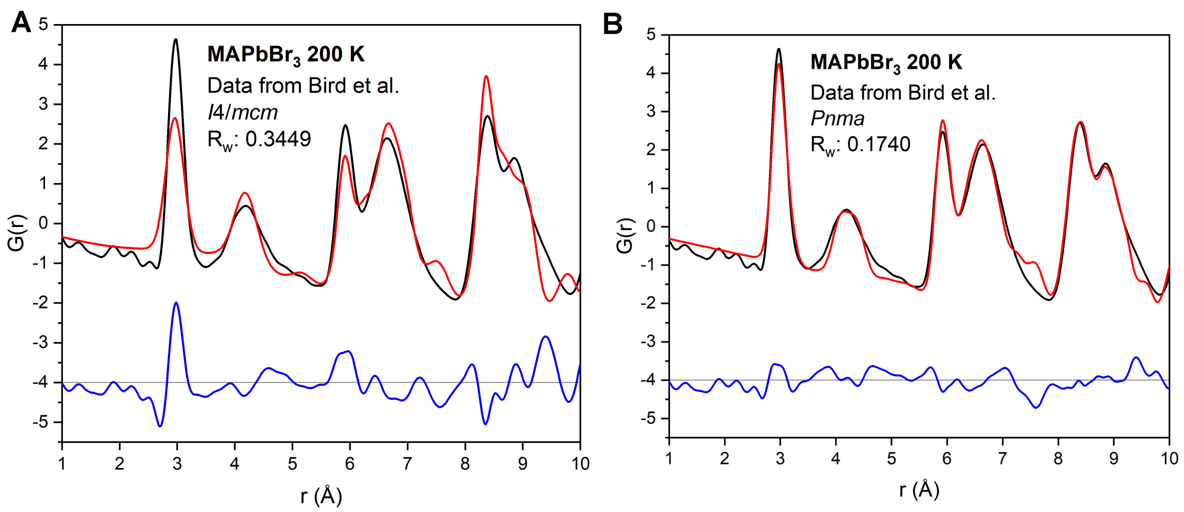

Figure 8. Short-range fit (r range = 1-10 Å) by using (A) the tetragonal $MAPbBr_3$ perovskite structure (I4/mcm) and (B) the orthorhombic $MAPbBr_3$ perovskite structure (Pnma). For the PDF fit (with PDFgui 1.0), the data from Bird *et al.*[17] at 200 K was used together with the fixed refinement results at 200 K from Bernasconi *et al.*[16]. In the PDF fit, only the scale and U_{iso} were refined.

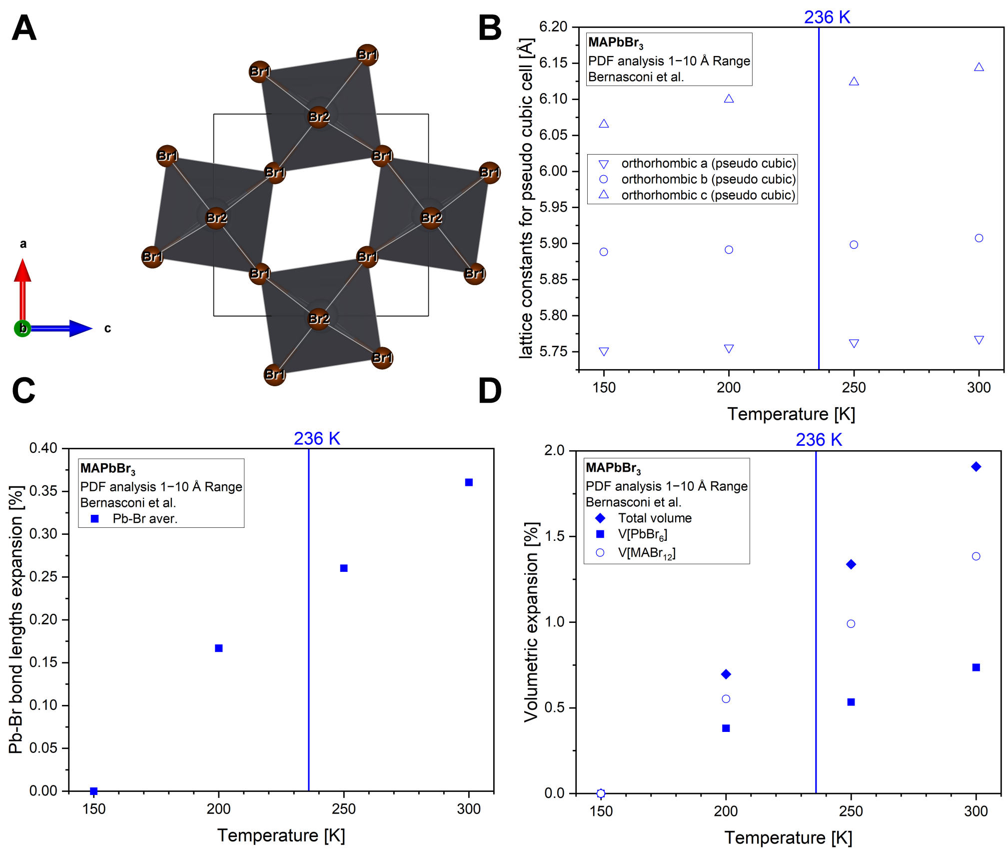

Figure 9. Results of the PDF analysis by Bernasconi *et al.*[16] using the G(r) range 1-10 Å with orthorhombic *Pnma* symmetry. (A) orthorhombic perovskite structure at 200 K; (B) orthorhombic lattice constants (pseudo-cubic); (C) averaged Pb-Br bond lengths expansion and (D) volumetric expansion of $MAPbBr_3$. Adapted with permission from Bernasconi *et al.*[16]. Copyright 2017 American Chemical Society.

A very similar behavior can also be observed in the data available for $MAPbBr_3$. Here, there is also no discontinuous change at small distances in the region of the o/t phase transformation (see figure 1 in Ref.[17]). In the PDF analyses available in the literature, it was observed for both $MAPbI_3$ and $MAPbBr_3$ that in the temperature range of the tetragonal and cubic phases, the low range up to 10 Å, can be best described by a short-range octahedra distortion, which essentially corresponds to the orthorhombic low temperature perovskite crystals structure for both $MAPbI_3$[14,17] and $MAPbBr_3$[15-17]. To illustrate and qualitatively reproduce this effect, PDF fits in the range of 1-10 Å are shown in Figure 8, using the $MAPbBr_3$ data at 200 K from Bird *et al.*[17] and the refinement results from Bernasconi *et al.*[16] (here, only the lead and bromine atoms were considered). In the PDF refinement only, the scaling and U_{iso} were refined. Similar to Bernasconi *et al.*, the use of the tetragonal *I*4/*mcm* perovskite structure (Figure 8A, R_w = 0.3449) leads to a poorer refinement than the use of the orthorhombic *Pnma* perovskite structure (Figure 8B, R_w = 0.1740)[16]. Although the results of the PDF analysis in Figure 8 show deviations (in the regions of r = 7 Å and r = 9.5 Å, there are peaks in the simulation that are not present in the data, and the peak at r = 4 Å is significantly off in thickness), the same qualitative results can be obtained with the experimental data of Bird *et al.*, and thus, the observations of Bernasconi *et al.* can be confirmed qualitatively[16,17]. The temperature-dependent lattice parameters, Pb-Br bond lengths and [$PbBr_6$] volumes determined by Bernasconi *et al.* using the orthorhombic perovskite structure in their PDF refinement for the range of 1-10 Å are shown in Figure 9[16]. Obviously, the thermal expansion of the local structure of $MAPbBr_3$ is fundamentally different from the thermal expansion of the averaged structure resulting from the analysis of the XRD data. The PDF refinement results from Bernasconi *et al.* show that all three orthorhombic lattice parameters increase with temperature, as do the Pb-Br bond lengths and [$PbBr_6$] volumes[16]. More recent structural PDF studies using symmetry-adapted PDF analysis (SAPA)[50] have investigated the local structure of ScF_3 and hybrid perovskites utilizing extended degrees of freedom (such as the "scissoring" mode X_5^+)[17,51].

Analysis of the anharmonic properties of the lead-halide bond with EXAFS

EXAFS spectroscopy is based on the ionization of an atom when an X-ray quantum is absorbed. This releases an electron whose kinetic energy depends on the energy of the X-rays. The released electron propagates as a matter wave and is scattered by neighboring atoms. Depending on the wavelength of the electron, constructive or destructive interference occurs between the outgoing wave and the backscattered waves. Because the energy of the X-rays is varied, the energy of the released electrons also changes and thus the corresponding wavelength of the electrons. This leads to alternating constructive and destructive interference and, thus, to a change in X-ray absorption depending on the energy, which corresponds to the fine structure of the X-ray absorption spectrum. These X-ray absorption changes can be measured in the energy range from just above the X-ray absorption edge up to a few hundred electron volts above it, i.e., in the upper range of the X-ray absorption edge (hence the term "extended" in EXAFS). From the shape and strength of the X-ray absorption changes, it is possible to deduce at what distance from the ionized atom it is scattered and to what extent, i.e., a so-called radial distribution function is obtained via Fourier transformation of the X-ray absorption "fine structure" data after normalization and background subtraction (for example with the Athena software)[52]. By comparing the scattering of electrons on and between neighboring atoms with simulations (for example, with the Artemis software)[6,52,53], the atomic distances of atom pairs R_{EXAFS} can be determined with high accuracy. However, the radial distribution function not only contains information about the atomic distances but also about the distance variations of the respective atom pairs, which corresponds to the parallel MSRD (EXAFS Debye-Waller factor or C_2). Since the lifetime of the EXAFS photoelectron (~10^{-15} s) is very short compared to the atomic vibrations (~10^{-12} s), and, at the same time, the limited mean free path of the EXAFS photoelectron is restricted to the local environment of the investigated atom, the anharmonic properties of the investigated bond pair can be studied very well[34]. The relative ΔC_2 (T) was fitted with an Einstein behavior by Schuck *et al.*[6] to determine parallel MSRD (T)[54] of $MAPbI_3$:

$$\text{parallel MSRD (T)} = \frac{\hbar^2}{\mu k_B}\frac{1}{2\theta_E}\coth\left(\frac{\theta_E}{2T}\right) \quad (2)$$

(μ: reduced mass, Θ_E: Einstein temperature). The resulting parallel MSRD (T) is shown in Figure 10A. This figure also shows the parallel MSRD (T) for $MAPbBr_3$, which was interpreted by Weadock *et al*. using both a correlated Debye model and an Einstein behavior [in the Debye model, a distinction was made between a low-temperature ($\Theta_{D,LT}$ = 148 K) and a high-temperature range ($\Theta_{D,LT}$ = 167 K)][7]. Weadock *et al*. noted that the Einstein temperatures for $MAPbI_3$ and $MAPbBr_3$ increase with decreasing reduced mass $\mu = m_1m_2/(m_1 + m_2)$, which corresponds to the relationship between the frequency and mass of an oscillator[7]. From Θ_E, a direct derivation of the effective force constant k_0 (bond-stretching effective force constant) could be made since the following applies:

$$k_0 = \Theta_E^2\mu = (\mu * 1.660539*10^{-27}\text{ kg} * (2\pi * \nu_E)^2)/16.022\ [\text{eV/Å}^2] \quad (3)$$

[1 N/m = 1/16.022 eV/Å²], [1 THz = 47.9924 K], and ν_E: Einstein frequency [THz] [Table 1].

From the temperature-dependent relative interatomic distances ΔR_{EXAFS} and the averaged relative interatomic distances ΔR_{XRD} resulting from the synchrotron XRD [Figure 11], Schuck *et al*. determine the relative "perpendicular MSRD" ($\Delta\langle\Delta u^2_{perp}\rangle$) for $MAPbI_3$, which correspond to vibrations perpendicular to the lead-halide bonding direction (bond-bending vibrations)[6].

The following relationship applied:[55]

$$\Delta\langle\Delta u^2_{perp}\rangle = 2 * R_{XRD}\,(\Delta R_{EXAFS} - \Delta R_{XRD}). \quad (4)$$

The absolute values of the perpendicular MSRD for $MAPbI_3$ were then obtained, analogously to the parallel MSRD, through fitting of $\Delta\langle\Delta u^2_{perp}\rangle$ with a correlated Einstein model[34]. The parallel MSRD values were fitted with two Einstein temperatures: one for the orthorhombic low-temperature range up to 160 K (LT), the other for the tetragonal high-temperature range up to 260 K (HT). This procedure leads to a solid explanation of the experimental values (also for the description of the γ_{EXAFS}-dependence [Figure 10B and C, Table 1]). The differing dimensionality ($\Delta u^2_{perp} = \Delta u^2_x + \Delta u^2_y$) compared to the parallel MSRD makes it necessary to use the following term:[33,34]

$$\langle\Delta u^2_{perp}\rangle(T) = \frac{\hbar^2}{\mu k_B}\frac{1}{\theta_{E(perp)}}\coth\left(\frac{\theta_{E(perp)}}{2T}\right) \quad (5)$$

Analogous to k_0, the corresponding perpendicular effective force constant $k_\perp$ (bond-bending effective force constant) from the correlated Einstein model could be calculated for $MAPbI_3$ [Table 1][6]. Analogous to the procedure for $MAPbI_3$, the relative perpendicular MSRD and the bond-bending effective force constant were also determined for $MAPbBr_3$ from the available data[7]. For $MAPbBr_3$, this was possible only for the tetragonal and cubic phases since the values determined for ΔR_{EXAFS} and ΔR_{XRD} in the orthorhombic phase [Figure 11], based on the results of Weadock *et al*., lead only to unphysical values for the relative perpendicular MSRD (here, the digitization of the data from Weadock *et al*. could not be carried out with sufficient accuracy for the orthorhombic phase)[7]. However, since the phase transformation from tetragonal to cubic is being discussed here, this is not limiting. The ratio γ_{EXAFS} = perpendicular MSRD/parallel MSRD

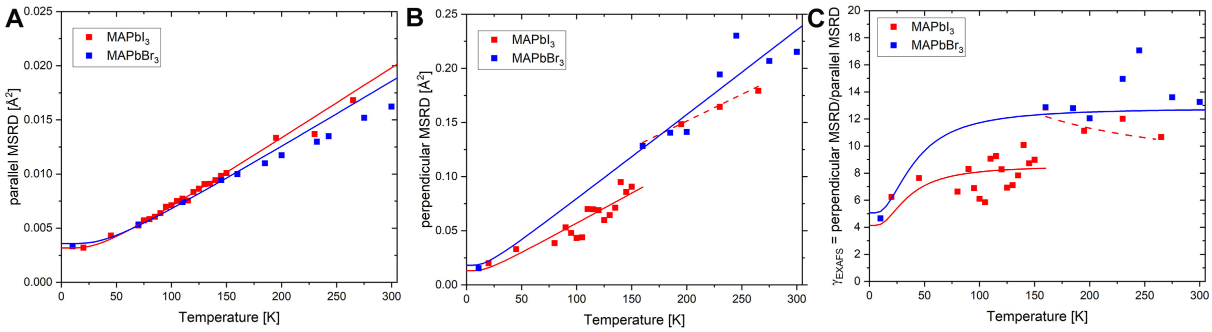

Figure 10. Temperature-dependent MSRDs: (A) parallel, (B) perpendicular and (C) γ_{EXAFS}. Red: $MAPbI_3$ (Schuck *et al.*[6]); blue: $MAPbBr_3$ (Weadock *et al.*[7]). Solid lines: Einstein fits. In (B) the parallel MSRD values for $MAPbI_3$ were fitted with two Einstein temperatures, one for the orthorhombic low-temperature range up to 160 K, the other for the tetragonal high-temperature range up to 260 K (here with an additional static component of 0.05). This procedure also leads to a better explanation of the experimental values for the description of the γ_{EXAFS} dependence in (C). Adapted with permission from Schuck *et al.*[6]. Copyright 2022 American Chemical Society.

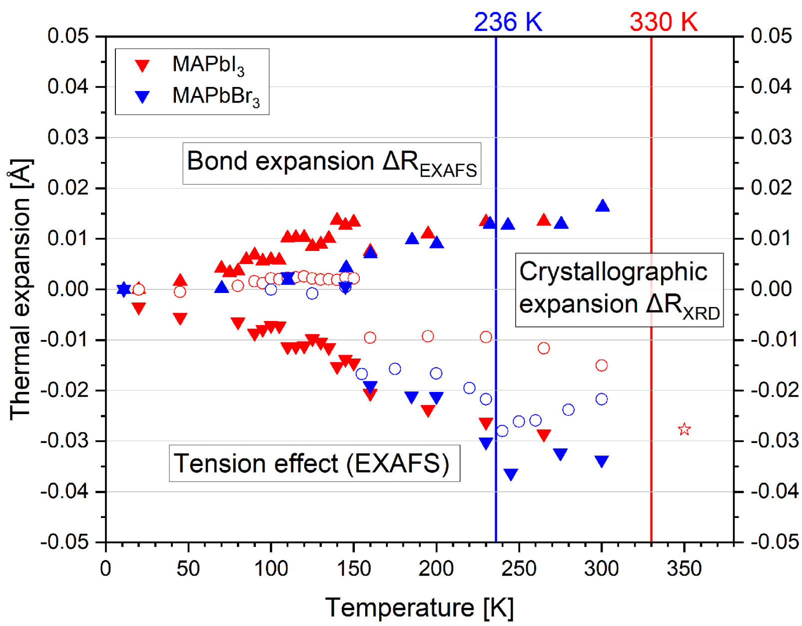

Figure 11. Relative Pb-X expansion of $MAPbI_3$ from Schuck *et al.*[6] (red) and $MAPbBr_3$ (Weadock *et al.*[7]) (blue). Positive bond expansion ΔR_{EXAFS} (solid upward triangles) and negative tension effect (solid downward triangles) result in the overall crystallographic expansion ΔR_{XRD} (open circles). Values for the cubic perovskite phase of $MAPbI_3$ are also given from Whitfield *et al.*[36] (open red star symbol). Adapted with permission from Schuck *et al.*[6]. Copyright 2022 American Chemical Society.

describes the degree of anisotropy of the relative vibrations [Figure 10C][34]. The uncertainties pointed out by Schuck *et al.* may be of a similar (if not larger) magnitude in the behavior of $MAPbBr_3$ shown here, so that the anisotropy of the relative vibrations and the perpendicular MSRD of $MAPbI_3$ and $MAPbBr_3$ are unlikely to differ significantly. However, perpendicular MSRD $<\Delta u^2_{perp}>$ (T) reveals the negative tension effect in the lead-halide bond [Figure 11][6]. Tension is defined as $-<\Delta u^2_{perp}>/2R_{XRD}$[56]. In the tetragonal/cubic phases of $MAPbI_3$ and $MAPbBr_3$, strong negative tension effects result in a shortening of R_{XRD}, which is accompanied by the observed negative changes in the partial volume of the [PbX_6] octahedra. Tenison effects are often used to explain the structural mechanism of NTE[57], and these tension effects are also associated with the behavior of optical phonons[58,59]. Although Dalba *et al.* point out that "in general the

Table 1. Einstein temperatures and frequencies for parallel ($\Theta_{E||}$, $\nu_{E||}$) and perpendicular MSRD ($\Theta_{E\perp}$, $\nu_{E\perp}$), bond-stretching effective force constant $k_{||}$ (corresponds to k_0), and bond-bending effective force constant $k_\perp$

	$MAPbI_3$ [6]	$MAPbBr_3$ [7]		
μ	78.702	57.666		
Pb-X bond-stretching				
$\Theta_{E||}$ [K]	97.0 (3)	117.3 (4)	$\Theta_{D||}$ [K]	LT: 148 (4); HT: 167 (5)
$\nu_{E||}$ [THz]	2.021 (5)	2.444 (6)	$\nu_{D||}$ [THz]	LT: 3.08 (8); HT: 3.48 (10)
$k_{||}$ [eV/Å^2]	1.315 (3)	1.410 (6)	$k_{||}$ [eV/Å^2]	LT: 1.43 (3); HT: 1.87 (5)
Pb-X bond-bending				
$\Theta_{E\perp}$ [K]	LT: 46.9 (8); HT: 50 (1)	HT: 46 (1)		
$\nu_{E\perp}$ [THz]	LT: 0.98 (2); HT: 1.04 (2)	HT: 0.96 (2)		
$k_\perp$ [eV/Å^2]	LT: 0.309 (6); HT: 0.348 (7)	HT: 0.218 (5)		

In each case, all values for the bond-stretching were determined for the orthorhombic phase (LT). For $MAPbBr_3$, the Debye temperatures and frequencies determined by Weadock *et al.*[7] are also given for the parallel MSRD in the orthorhombic phase (LT) and the tetragonal/cubic temperature range (HT).

Einstein frequencies cannot be correlated in a simple way to the phonon density of states"[60], the same authors draw parallels between the relative atomic vibrations of EXAFS and optical phonons[60,61].

Also, an attempt is made here to establish correlations between the relative atomic vibrations obtained from EXAFS studies on one hand and the behavior of optical phonons on the other. In addition, the Grüneisen parameters of individual phonon modes (also known as phonon deformation potentials) are of interest as a probe of the anharmonicity associated with phonon-phonon scattering and heat transport[59,62,63]. Two recent publications investigated the temperature dependence of optical phonons using infrared (IR) and terahertz measurements of $MAPbI_3$ and $MAPbBr_3$[64,65]. Two optical phonons at around 0.9 and 1.8 THz have been reported from Boldyrev *et al.* in $MAPbI_3$ single crystals using temperature-dependent (figure 5 in Ref.[64]), high-resolution terahertz reflection spectroscopy[64]. The authors of the study attribute both modes to the inorganic $[PbI_6]$ framework structure, with the low-frequency mode dominated by bending modes, while stretching processes play a larger role in the higher-frequency mode. Both modes observed from Boldyrev *et al.* show parallels to the bond-stretching frequencies of $\nu_{E||} = 2$ THz and to the bond-bending frequency of $\nu_{E\perp} = 1$ THz for $MAPbI_3$ both observed with EXAFS[64]. In a similar temperature-dependent time-domain THz transmission and far IR reflectance investigation on optical phonons in $MAPbBr_3$ single crystals, the higher frequency mode measured by Železný *et al.* shows an increase in the frequency in the tetragonal phase from approx[65]. 2.07 THz to approx. 2.12 THz (figure 5 in Ref.[65]), which corresponds to a negative mode Grüneisen parameter for this mode. In contrast, the low-frequency mode at 1.4 THz observed by Železný *et al.* shows hardly any temperature dependence[65]. The similarities to the EXAFS results of $MAPbBr_3$ are also present here as the bond-stretching frequencies of $\nu_{E||} = 2.4$ THz and the bond-bending frequency of $\nu_{E\perp} = 1$ THz for $MAPbBr_3$ are observed with EXAFS. Note the frequency increase in the EXAFS results; for $MAPbBr_3$, the bond-stretching frequencies determined with a Debye model are lower in the low-temperature range (3.1 THz) than in the high-temperature range (3.5 THz). This frequency increase can also be observed, although to a lesser extent, in the bond-stretching frequencies for $MAPbI_3$.

CONCLUSION

The review of the results from the analysis of the averaged crystal structure with XRD diffraction methods shows temperature-dependent changes in the tetragonal phase with an apparent shortening of the Pb-X bonds and an apparent shrinkage of the $[PbX_6]$ octahedra in both $MAPbI_3$ and $MAPbBr_3$ with increasing temperature up to the cubic phase. The thermal expansion can best be described with the linear thermal expansion coefficient $\alpha_{[averaged]}$ for the averaged tetragonal lattice constant $a_{averaged} = ((2^*a_{tet})+c_{tet})/3$ since the lowest temperature dependence occurs for this expansion coefficient. Using the Grüneisen tensor, positive Grüneisen parameters $\gamma_{[001]}$ and $\gamma_{[100]}$ can be expected for nearly the complete temperature range of the tetragonal phase of $MAPbI_3$ (with the exception of $\gamma_{[001]}$ in a small temperature range close to the cubic phase transition above 307 K). The analysis of the tetragonal/cubic phase transformation using the standard Landau theory treatment seems to show a certain variance in the determination of the order parameters, but this can probably largely be explained by the quality of the underlying structure refinements. From the point of view of the local structure, it is remarkable that the thermal expansion of the very local arrangement of the lead halide octahedra is apparently unaffected by the tetragonal/cubic phase transformation. The temperature-dependent changes in the range of 150-300 K of the Pb-Br bond distances determined for $MAPbBr_3$ by Bernasconi *et al*. from PDF refinements in the range of 1-10 Å using the orthorhombic *Pnma* perovskite crystal structure are of approximately the same order of magnitude as the bond expansion values ΔR_{EXAFS} determined by Weadock *et al*. with EXAFS[7,16]. Tension effects are observed with EXAFS in the tetragonal phase for both $MAPbI_3$ and $MAPbBr_3$. The positive bond extension and the negative tension effects of the lead-halide bond are approximately the same in $MAPbI_3$ (and presumably also in $MAPbBr_3$) in the orthorhombic phase. After the transition to the tetragonal phase, the equilibrium shifted in favor of the negative tension effects in both $MAPbI_3$ and $MAPbBr_3$. Further analysis of similarities between EXAFS relative atomic vibrations and optical phonon studies could be a rewarding way to better understand the thermal expansion in the tetragonal perovskite structure of $MAPbI_3$ and $MAPbBr_3$. This brief overview of the thermal expansion of $MAPbI_3$ and $MAPbBr_3$ can hopefully contribute to a more comprehensive description that includes all relevant inorganic halide perovskites and the discussion of NTE coefficients for ferroelectric oxide perovskites.

DECLARATIONS

Authors' contributions

Contributed equally to this article: Schuck G, Többens DM, Schorr S

Availability of data and materials

Not applicable.

Financial support and sponsorship

None.

Conflicts of interest

All authors declared that there are no conflicts of interest.

Ethical approval and consent to participate

Not applicable.

Consent for publication

Not applicable.

REFERENCES

1. Chouhan L, Ghimire S, Subrahmanyam C, Miyasaka T, Biju V. Synthesis, optoelectronic properties and applications of halide perovskites. *Chem Soc Rev* 2020;49:2869-85. DOI
2. Pérez-Fidalgo L, Xu K, Charles BL, et al. Anomalous electron-phonon coupling in cesium-substituted methylammonium lead iodide perovskites. *J Phys Chem C* 2023;127:22817-26. DOI
3. Spera EL, Pereyra CJ, Gau DL, Berruet M, Marotti RE. Excitonic optical properties of $CH_3NH_3PbI_3$ perovskite and its dependence with temperature. *MRS Adv* 2024;9:39-44. DOI
4. Jošt M, Kegelmann L, Korte L, Albrecht S. Monolithic perovskite tandem solar cells: a review of the present status and advanced characterization methods toward 30% efficiency. *Adv Energy Mater* 2020;10:1904102. DOI
5. Duan L, Walter D, Chang N, et al. Stability challenges for the commercialization of perovskite-silicon tandem solar cells. *Nat Rev Mater* 2023;8:261-81. DOI
6. Schuck G, Többens DM, Wallacher D, Grimm N, Tien TS, Schorr S. Temperature-dependent EXAFS measurements of the Pb L3-edge allow quantification of the anharmonicity of the lead-halide bond of chlorine-substituted methylammonium (MA) lead triiodide. *J Phys Chem C* 2022;126:5388-402. DOI
7. Weadock NJ, Mackeen C, Qin X, et al. Thermal contributions to the local and long-range structural disorder in $CH_3NH_3PbBr_3$. *PRX Energy* 2023;2:033004. DOI
8. Schuck G, Lehmann F, Ollivier J, Mutka H, Schorr S. Influence of chloride substitution on the rotational dynamics of methylammonium in $MAPbI_{3-x}Cl_x$ perovskites. *J Phys Chem C* 2019;123:11436-46. DOI
9. Miyata K, Atallah TL, Zhu XY. Lead halide perovskites: crystal-liquid duality, phonon glass electron crystals, and large polaron formation. *Sci Adv* 2017;3:e1701469. DOI PubMed PMC
10. Tailor NK, Satapathi S. Crystalline-liquid duality of specific heat in halide perovskite semiconductor. *Scr Mater* 2023;223:115061. DOI
11. Adams DJ, Churakov SV. Classification of perovskite structural types with dynamical octahedral tilting. *IUCrJ* 2023;10:309-20. DOI PubMed PMC
12. Liang X, Klarbring J, Baldwin WJ, Li Z, Csányi G, Walsh A. Structural dynamics descriptors for metal halide perovskites. *J Phys Chem C Nanomater Interfaces* 2023;127:19141-51. DOI PubMed PMC
13. Weadock NJ, Sterling TC, Vigil JA, et al. The nature of dynamic local order in $CH_3NH_3PbI_3$ and $CH_3NH_3PbBr_3$. *Joule* 2023;7:1051-66. DOI
14. Beecher AN, Semonin OE, Skelton JM, et al. Direct observation of dynamic symmetry breaking above room temperature in methylammonium lead iodide perovskite. *ACS Energy Lett* 2016;1:880-7. DOI
15. Page K, Siewenie JE, Quadrelli P, Malavasi L. Short-range order of methylammonium and persistence of distortion at the local scale in $MAPbBr_3$ hybrid perovskite. *Angew Chem Int Ed* 2016;55:14320-4. DOI PubMed
16. Bernasconi A, Malavasi L. Direct evidence of permanent octahedra distortion in $MAPbBr_3$ hybrid perovskite. *ACS Energy Lett* 2017;2:863-8. DOI
17. Bird TA, Chen J, Songvilay M, et al. Large dynamic scissoring mode displacements coupled to band gap opening in hybrid perovskites. *arXiv* 2021. Available from: https://arxiv.org/abs/2108.05751 [Last accessed on 7 Aug 2024].
18. Simenas M, Gagor A, Banys J, Maczka M. Phase transitions and dynamics in mixed three- and low-dimensional lead halide perovskites. *Chem Rev* 2024;124:2281-326. DOI PubMed PMC
19. Kutes Y, Ye L, Zhou Y, Pang S, Huey BD, Padture NP. Direct observation of ferroelectric domains in solution-processed $CH_3NH_3PbI_3$ perovskite thin films. *J Phys Chem Lett* 2014;5:3335-9. DOI PubMed
20. Bari M, Bokov AA, Ye Z. Ferroelastic domains and phase transitions in organic-inorganic hybrid perovskite $CH_3NH_3PbBr_3$. *J Mater Chem C* 2021;9:3096-107. DOI
21. Bari M, Bokov AA, Leach GW, Ye Z. Ferroelastic domains and effects of spontaneous strain in lead halide perovskite $CsPbBr_3$. *Chem Mater* 2023;35:6659-70. DOI
22. Wilson JN, Frost JM, Wallace SK, Walsh A. Dielectric and ferroic properties of metal halide perovskites. *APL Mater* 2019;7:010901. DOI
23. Breternitz J. The “ferros” of $MAPbI_3$: ferroelectricity, ferroelasticity and its crystallographic foundations in hybrid halide perovskites. *Cryst Mater* 2022;237:135-40. DOI
24. Ambrosio F, De Angelis F, Goñi AR. The ferroelectric-ferroelastic debate about metal halide perovskites. *J Phys Chem Lett* 2022;13:7731-40. DOI PubMed PMC
25. Zheng W, Wang X, Zhang X, et al. Emerging halide perovskite ferroelectrics. *Adv Mater* 2023;35:e2205410. DOI
26. Haeger T, Heiderhoff R, Riedl T. Thermal properties of metal-halide perovskites. *J Mater Chem C* 2020;8:14289-311. DOI
27. Jacobsson TJ, Schwan LJ, Ottosson M, Hagfeldt A, Edvinsson T. Determination of thermal expansion coefficients and locating the temperature-induced phase transition in methylammonium lead perovskites using X-ray diffraction. *Inorg Chem* 2015;54:10678-85. DOI PubMed
28. Bozec Y, Kaang S, Hine P, Ward I. The thermal-expansion behaviour of hot-compacted polypropylene and polyethylene composites. *Composit Sci Technol* 2000;60:333-44. DOI
29. Becker P, Scyfried P, Siegert H. The lattice parameter of highly pure silicon single crystals. *Z Physik B Condens Matter* 1982;48:17-21. DOI

30. Ge C, Hu M, Wu P, et al. Ultralow thermal conductivity and ultrahigh thermal expansion of single-crystal organic-inorganic hybrid perovskite $CH_3NH_3PbX_3$ (X = Cl, Br, I). *J Phys Chem C* 2018;122:15973-8. DOI
31. Zhou Y, Guo Z, Qaid SMH, Xu Z, Zhou Y, Zang Z. Strain engineering toward high-performance formamidinium-based perovskite solar cells. *Solar RRL* 2023;7:2300438. DOI
32. Katan C, Mohite AD, Even J. Entropy in halide perovskites. *Nat Mater* 2018;17:377-9. DOI PubMed
33. Fornasini P, Grisenti R. On EXAFS debye-waller factor and recent advances. *J Synchrotron Rad* 2015;22:1242-57. DOI PubMed
34. Sanson A. EXAFS spectroscopy: a powerful tool for the study of local vibrational dynamics. *Microstructures* 2021;1:2021004. DOI
35. Schuck G, Többens DM, Koch-müller M, Efthimiopoulos I, Schorr S. Infrared spectroscopic study of vibrational modes across the orthorhombic-tetragonal phase transition in methylammonium lead halide single crystals. *J Phys Chem C* 2018;122:5227-37. DOI
36. Whitfield PS, Herron N, Guise WE, et al. Structures, phase transitions and tricritical behavior of the hybrid perovskite methyl ammonium lead iodide. *Sci Rep* 2016;6:35685. DOI PubMed PMC
37. Franz A, Többens DM, Schorr S. Interaction between cation orientation, octahedra tilting and hydrogen bonding in methylammonium lead triiodide. *Cryst Res Technol* 2016;51:534-40. DOI
38. Stoumpos CC, Malliakas CD, Kanatzidis MG. Semiconducting tin and lead iodide perovskites with organic cations: phase transitions, high mobilities, and near-infrared photoluminescent properties. *Inorg Chem* 2013;52:9019-38. DOI PubMed
39. Celeste A, Capitani F. Hybrid perovskites under pressure: present and future directions. *J Appl Phys* 2022;132:220903. DOI
40. Szafrański M, Katrusiak A. Mechanism of pressure-induced phase transitions, amorphization, and absorption-edge shift in photovoltaic methylammonium lead iodide. *J Phys Chem Lett* 2016;7:3458-66. DOI PubMed
41. Gil-González E, Pérez-Maqueda LA, Sánchez-Jiménez PE, Perejón A. Paving the way to establish protocols: modeling and predicting mechanochemical reactions. *J Phys Chem Lett* 2021;12:5540-6. DOI PubMed PMC
42. Whitfield PS, Herron N, Guise WE, et al. Correction: Corrigendum: structures, phase transitions and tricritical behavior of the hybrid perovskite methyl ammonium lead iodide. *Sci Rep* 2017;7:42831. DOI PubMed PMC
43. Schorr S, Sheptyakov D. Low-temperature thermal expansion in sphalerite-type and chalcopyrite-type multinary semiconductors. *J Phys Condens Matter* 2008;20:104245. DOI
44. Haussühl S. Kristallphysik; Weinheim, Germany: Physic-Verlag; 1983.
45. Feng J. Mechanical properties of hybrid organic-inorganic $CH_3NH_3BX_3$ (B = Sn, Pb; X = Br, I) perovskites for solar cell absorbers. *APL Mater* 2014;2:081801. DOI
46. Campbell BJ, Stokes HT, Tanner DE, Hatch DM. *ISODISPLACE*: a web-based tool for exploring structural distortions. *J Appl Cryst* 2006;39:607-14. DOI
47. Liu J, Du J, Phillips AE, Wyatt PB, Keen DA, Dove MT. Neutron powder diffraction study of the phase transitions in deuterated methylammonium lead iodide. *J Phys Condens Matter* 2022;34:145401. DOI PubMed
48. Egami T, Billinge SJL. Underneath the bragg peaks: structural analysis of complex materials; Oxford: Elsevier; 2003.
49. Billinge SJ. Nanoscale structural order from the atomic pair distribution function (PDF): there's plenty of room in the middle. *J Solid State Chem* 2008;181:1695-700. DOI
50. Bird TA, Herlihy A, Senn MS. Symmetry-adapted pair distribution function analysis (SAPA): a novel approach to evaluating lattice dynamics and local distortions from total scattering data. *J Appl Cryst* 2021;54:1514-20. DOI PubMed PMC
51. Bird TA, Woodland-Scott J, Hu L, et al. Anharmonicity and scissoring modes in the negative thermal expansion materials ScF_3 and $CaZrF_6$. *Phys Rev B* 2020;101:064306. DOI
52. Ravel B, Newville M. *ATHENA*, *ARTEMIS*, *HEPHAESTUS*: data analysis for X-ray absorption spectroscopy using *IFEFFIT*. *J Synchrotron Rad* 2005;12:537-41. DOI PubMed
53. Bunker G. Application of the ratio method of EXAFS analysis to disordered systems. *Nucl Instrum Methods Phys Res* 1983;207:437-44. DOI
54. Bunker G. Introduction to EXAFS; Cambridge: Cambridge University Press; 2010.
55. Fornasini P, a Beccara S, Dalba G, et al. Extended X-ray-absorption fine-structure measurements of copper: local dynamics, anharmonicity, and thermal expansion. *Phys Rev B* 2004;70:174301. DOI
56. Fornasini P, Grisenti R. The coefficient of bond thermal expansion measured by extended X-ray absorption fine structure. *J Chem Phys* 2014;141:164503. DOI PubMed
57. Fornasini P. Vibrational anisotropy. In: Schnohr CS, Ridgway MC, editors. X-ray absorption spectroscopy of semiconductors. Berlin: Springer; 2015. pp. 127-42. DOI
58. Attfield JP. Mechanisms and materials for NTE. *Front Chem* 2018;6:371. DOI PubMed PMC
59. Dove MT, Fang H. Negative thermal expansion and associated anomalous physical properties: review of the lattice dynamics theoretical foundation. *Rep Prog Phys* 2016;79:066503. DOI PubMed
60. Dalba G, Diop D, Fornasini P, Rocca F. An EXAFS study of thermal disorder in GaAs. *J Phys Condens Matter* 1994;6:3599-608. DOI
61. Dalba G, Fornasini P, Kuzmin A, Purans J, Rocca F. X-ray absorption spectroscopy study of ReO_3 lattice dynamics. *J Phys Condens Matter* 1995;7:1199-213. DOI
62. Talit K, Strubbe DA. Stress effects on vibrational spectra of a cubic hybrid perovskite: a probe of local strain. *J Phys Chem C* 2020;124:27287-99. DOI
63. Gava V, Martinotto AL, Perottoni CA. First-principles mode Gruneisen parameters and negative thermal expansion in α-ZrW_2O_8. *Phys*

Rev Lett 2012;109:195503. DOI PubMed

64. Boldyrev KN, Anikeeva VE, Semenova OI, Popova MN. Infrared spectra of the $CH_3NH_3PbI_3$ hybrid perovskite: signatures of phase transitions and of organic cation dynamics. *J Phys Chem C* 2020;124:23307-16. DOI
65. Železný V, Kadlec C, Kamba S, Repček D, Kundu S, Saidaminov MI. Infrared and terahertz studies of phase transitions in the $CH_3NH_3PbBr_3$ perovskite. *Phys Rev B* 2023;107:174113. DOI